Competition between photodetachment and photodissociation in O2−

Laura Dinu, Gerrit C. Groenenboom, and Wim J. van der Zande

Citation: J. Chem. Phys. **119**, 8864 (2003); doi: 10.1063/1.1615517
View online: http://dx.doi.org/10.1063/1.1615517
View Table of Contents: http://jcp.aip.org/resource/1/JCPSA6/v119/i17
Published by the AIP Publishing LLC.

Competition between photodetachment and photodissociation in O_2^-

Laura Dinu[a)]
FOM—Institute for Atomic and Molecular Physics (AMOLF), Kruislaan 407, 1098 SJ Amsterdam, The Netherlands

Gerrit C. Groenenboom
Institute of Theoretical Chemistry, University of Nijmegen, Toernooiveld 1, 6525 ED Nijmegen, The Netherlands

Wim J. van der Zande
FOM—Institute for Atomic and Molecular Physics (AMOLF), Kruislaan 407, 1098 SJ Amsterdam, The Netherlands and Department of Molecule and Laser Physics, University of Nijmegen, Toernooiveld 1, 6525 ED Nijmegen, The Netherlands

(Received 14 July 2003; accepted 12 August 2003)

Using fast beam photofragment spectroscopy, we have studied the competition between photodissociation and photodetachment in O_2^-. The photodissociation fraction is ~10% and increases somewhat between 285 and 266 nm. High resolution photofragment spectroscopy shows that the O_2^- beam is composed of $v=0$ ions only. The photofragment angular distribution has an anisotropy parameter $\beta=1.9$, indicating that the process of dissociation has a parallel character, attributed to the $A\,^2\Pi_u \leftarrow X\,^2\Pi_g$ transition. A detailed analysis of the kinetic energy release of the photofragments shows the structure related to the distribution over the six fine-structure dissociation limits $O^-(^2P_{3/2,1/2})+O(^3P_{2,1,0})$. The results are compared with an analytical diabatic dissociation model, taking into account the long range charge–quadrupole interactions; the $A\,^2\Pi_u$ is described in a Born–Oppenheimer electrostatic aproximation and projected onto the different fine-structure states at large internuclear separation using analytical expressions derived from the long range charge–quadrupole interactions between O^- and O fragments. © *2003 American Institute of Physics.* [DOI: 10.1063/1.1615517]

I. INTRODUCTION

The O_2^- is a stable molecular ion. It has an electron affinity of 0.43 eV.[1,2] From Raman spectroscopy and autodetachment experiments, the vibrational constant is determined to be 1090 cm^{-1}.[3,4] The addition of an extra electron to the $^3\Sigma_g^-$ electronic ground in the antibonding π_g orbital state weakens the chemical bond and increases the equilibrium separation from 1.2075 Å in O_2 to 1.346 Å in O_2^-.[2,5] The ground state of the anion is of inverted $^2\Pi_g$ symmetry with a fine-structure constant $A=-20\pm2$ meV.[2] In contrast to its neutral counterpart, the anion O_2^- has low lying excited states that are coupled to the ground state via allowed dipole transitions. In fact, the first excited state is the $A\,^2\Pi_u$ state,[6,7] which is bound with respect to the first dissociation limit $O(^3P_2)+O^-(^2P_{3/2})$. The significant difference between the electron affinities of the O_2 molecule (0.43 eV) and the O atom (1.461 eV)[8–10] shifts the threshold for the photodissociation of O_2^- with respect to that of O_2 from 243 (5.1 eV) to 304 nm (4.08 eV). In planetary atmospheres, the photodissociation of O_2^- may be both a source of oxygen atoms and ions. In addition to this, O_2^- is a far more efficient absorber of near-UV radiation than neutral oxygen. The superoxide anion O_2^- is considered to be the most important anion involved in the negative ion chemistry in the lower ionosphere.[11] Together with the O^- anion, O_2^- is at the base of a chain of chemical reactions leading to more complex negative ions.

Whereas the photodetachment of O_2^- has been studied in great detail, providing absolute cross sections, photoelectron angular distributions, and the observation of resonant states,[1–5,12–14] the photodissociation of O_2^- has not received much attention. To the best of our knowledge, the photodissociation of O_2^- was first observed by Vestal and Mauclaire[15] in a tandem quadrupole mass spectrometer. They reported a cross section of 4.2×10^{-19} cm^2 for the photodissociation of O_2^- into $O+O^-$ at 4.07±0.07 eV. More recently, the photodissociation of O_2^- has been studied by Johnson and co-workers.[4,16] These studies extended the investigation to a wavelength range 3.5–5.6 nm and reported a 3% branching of dissociation relative to direct electron photodetachment. Furthermore, the angular distribution of the ejected O^- corresponds to an anisotropy parameter $\beta=1.2\pm0.1$. These authors identified the $A\,^2\Pi_u$ electronic excited state as being involved in the photodissociation process. Dissociative attachment studies ($O_2+e^-\rightarrow O_2^-{}^*\rightarrow O+O^-$) indicate a $^2\Pi_u$ state as an intermediate state.[17,18] Also, theoretical studies on the potential energy curves of O_2^- paid special attention to the $A\,^2\Pi_u$ state.[6,19–21]

In the present study, we have applied high resolution fast beam photofragment spectroscopy on O_2^- molecular ions produced in a continuous hollow-cathode discharge ion source. The kinetic energy of the $O–O^-$ fragment pairs is

[a)]Electronic mail: ldinu@amolf.nl

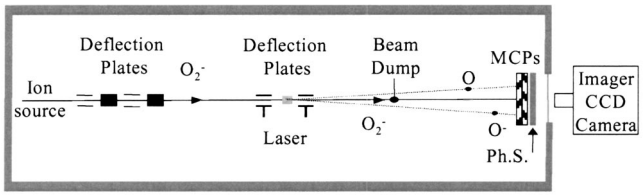

FIG. 1. Scheme of the experimental setup. A continuous molecular ion beam of O_2^- is crossed with a 25 Hz laser pulse (266–285 nm). PDE and PDI occur leading to O_2, O, and O^- fragments. The use of the beam dump is optional as well as the deflection plates after the laser interaction region. The double exposure camera detects position (x and y coordinates) and the relative arrival time difference of the fragments onto the MCP's.

determined with sufficient resolution to assign unambiguously the initial vibrational state of the O_2^- ions. The final kinetic energy of the fragments is affected by the fine-structure splitting of the $O_2^-(^2\Pi_{g,\Omega})$ $(\Omega=3/2,1/2)$ ground state, and the fine structure splitting of the $O^-(^2P_{3/2,1/2})$ and the $O(^3P_{2,1,0})$ fragments. The highly structured kinetic energy release (KER) spectrum makes it possible to estimate the branching over the six possible dissociation limits. The results are compared to a calculation assuming a diabatic model in the transition between the long range where the interaction energies are dominated by the charge–quadrupole interaction between the fragments to the asymptotic region, where the atomic spin–orbit interaction dominates over the long range electrostatic interaction. The angular distribution of the O fragments has an anisotropy parameter $\beta=1.9$, a value that it is considerably closer to 2 than previously reported. The competition between the photodetachment (PDE) and photodissociation (PDI) is determined by detecting the O_2 products from PDE and the O atoms from the PDI process on the same detector in the pulse counting mode. We find PDI/(PDI+PDE)~10%. Clearly, the photodissociation of O_2^- and hence the formation of O^- at wavelengths of less than 300 nm should not be ignored in ionospheric models.

II. METHODS:

A. Experiment

A continuous molecular beam of O_2^- is extracted at 5 keV from a hollow-cathode discharge ion source. The discharge is maintained at 600 V and 20 mA. The temperature of the source is ~350 K. We optimized the O_2^- signal by introducing molecular nitrogen in the discharge chamber. The most important reactions describing the production of negative molecular oxygen ions in the source are $O_2+O_2+e\rightarrow O_2^-+O_2$ and $N_2+O_2+e\rightarrow O_2^-+N_2$. The superoxide ions O_2^- are mass selected by a Wien filter and introduced in a fast beam setup (see Fig. 1). By means of four deflection plates, the beam is guided through the apertures of the apparatus. Two Einzel lenses are used to focus the beam through the exit aperture of the ion source region and to reduce the radial size of the beam in the region of interaction with the laser.

The O_2^- anion beam is crossed perpendicular by ultraviolet laser radiation. The laser system used for this experiment consists of a 50 Hz Spectra Physics Nd-YAG laser pumping a Lambda Physik ScanMate dye laser. The 532 nm output of the Nd-YAG laser or the output of the ScanMate (around 560 nm) is frequency doubled in a BBO nonlinear crystal. The UV laser radiation (266 nm or 275–285 nm) is focused in the setup in a region of $1\times1\times1$ mm^3 (x,y,z). The UV laser energy, measured after the interaction region, is ~2 mJ. The polarization of the laser is chosen to be parallel to the detector surface.

The photodetachment signal consists of neutral O_2 molecules flying in the same direction as the initial O_2^- beam. The photodissociation signal, on the other hand, consists of O and O^- fragments scattering out of the parent ion beam due to the kinetic energy released in the dissociation process. After a time-of-flight of ~7 μs the fragments reach a detector consisting of two microchannelplates (MCPs) and a P46-phosphor screen. Outside the vacuum system, a double exposure CCD camera (LaVision, modified Imager3 VGA) records the images of the phosphor screen, from which the positions (x,y) and arrival time t of the detected fragments are obtained.[22,23] In brief, the camera records the image of the phosphor screen and the intensity of the spots corresponding to individual particles. Due to the fast interline transfer of the CCD chip, the camera is capable of taking two successive images of the same phosphor decay for each event that originates from a single laser pulse. Subsequently, the arrival time is deduced for each event from the ratio of intensities measured in both images.[24] Therefore, this camera retrieves not only the (x,y) coordinates of the spots (~80 μm resolution) but also the arrival time of the particles (~1 ns resolution).

The positions and arrival time difference between the two fragments resulting from a dissociation event are used to determine the orientation of the molecule during the dissociation process and to calculate the kinetic energy released in the process. Multiple dissociation events per laser shot can be detected, since coincident fragments have a center-of-mass position in the middle of the detector. The camera is the master clock of the experiment. It controls the firing of the laser and it limits the acquisition rate to 25 Hz.

B. Theory: A diabatic model for the correlated fine-structure branching ratios

The Franck–Condon region of the ground state of the O_2^- ion is well described by adiabatic Born Oppenheimer (ABO) potentials, i.e., determined by the eigenvalues of the usual Coulomb Hamiltonian $\hat{H}_{\mathrm{Coul}}$. In this region, the projection of the electronic orbital angular momentum on the molecular axis (Λ) is a good quantum number. The fine-structure splittings are much smaller than the binding energies derived in the ABO potentials. Since $\hat{H}_{\mathrm{Coul}}$ does not contain the spin, all the ABO states correlating with the $O^-(^2P)+O(^3P)$ dissociation limit are asymptotically degenerate. Near the dissociation limit at the long range, the spin–orbit coupling $\hat{H}_{\mathrm{SO}}$ dominates the interaction among these states. Between the Franck–Condon region and the asymptotic region, a region exists, in which the charge–

quadrupole, ion-atom interaction between the fragments is still significantly larger than the asymptotic atomic fine-structure interactions.

In the case of dissociation at very small recoil velocity the atomic fine-structure branching is best described by a spin–orbit adiabatic correlation diagram with Hund's case-*c* potentials. These potentials follow from the eigenvalues of $\hat{H}_{\mathrm{Coul}}+\hat{H}_{\mathrm{SO}}$. The associated eigenfunctions are labeled by Ω, the projection of the total electronic angular momentum on the molecular axis, rather than Λ. Since the $A\,^2\Pi_{u,3/2}$ and $A\,^2\Pi_{u,1/2}$ states are the lowest $^2\Pi_u$ states for $\Omega=3/2$, 1/2, respectively, they both correlate with the lowest $O^-(^2P_{3/2})+O(^3P_2)$ limit. However, at the wavelengths used in this experiment, the recoil kinetic energy (approximately 500 meV) is much larger than the atomic fine-structure energy differences. Thus, this adiabatic model does not necessarily apply in the energy regime of our experiment.

In the high-energy limit a diabatic or sudden model is expected to apply. The long range states are derived from a correlation diagram for the ABO states. In the present case, it is assumed that in the long range the molecular potentials are well described by the charge–quadrupole interaction. The diabatic wave function is projected onto a basis of product atomic fine-structure states in order to obtain the atomic fine structure distribution. A problem treating molecular dissociation to asymptotic fine-structure states was worked out with a similar analytic diabatic model for the photodissociation of neutral O_2 in the Herzberg region.[29,30] A similar treatment has been used in the experimental paper of Leahy *et al.*,[31] which was based on the theory from Singer *et al.*[32]

The present treatment is different in two ways from the earlier. Dealing with an anion, the leading long range term is the charge–quadrupole interaction, which is stronger than the quadrupole–quadrupole interaction as, for example, in neutral O_2. Second, the use of the long range interactions makes the full treatment analytical without using empirical parameters, as in Refs. 31, 32.

Using the notation of Ref. 30, we express the orbital part of the ABO functions in the long range as product atomic wave functions,

$$|l_a\lambda_a\rangle|l_b\lambda_b\rangle, \tag{1}$$

where the subscript *a* refers to the O^- ion and *b* to the neutral O atom, $l_a=l_b=1$, and $\Lambda=\lambda_a+\lambda_b=1$ for Π states. The neutral O_2 ABO states can be obtained by a Clebsch–Gordon coupling of the atom states. However, for O_2^- it is more convenient to work in the uncoupled basis, since the charge–quadrupole interaction $V^{(0,2)}$ lifts the degeneracy of the $|11\rangle|10\rangle$ and $|10\rangle|11\rangle$ states and the off-diagonal matrix element between the states is zero.

A complication arises from the fact that two $^2\Pi_u$ states exist for each value of Ω correlating with the $O^-(^2P)+O(^3P)$ limit. In order to determine the wave function for the lowest state, i.e., the one correlating with the *A* state, we must consider the leading nonvanishing long range term in the multipole expansion of $\hat{H}_{\mathrm{Coul}}$. A calculation shows that the $|10\rangle|11\rangle$ state, i.e., the state with $\lambda_O=1$, is the lowest. This can be readily understood qualitatively, since the $2p$ shell electron configurations of the $O(^3P)$ atom for $\lambda_O=1$ and $\lambda_O=0$ are $|p_{-1}p_0p_1\overline{p_1}|$ and $|p_{-1}p_0\overline{p_0}p_1|$, respectively. The $\lambda_O=0$ configuration is higher in energy, since it has an extra electron in the p_0 orbital, which is pointing toward the O^-.

The ABO wave function is completed by adding a Clebsch–Gordon coupled atomic spin part (see Ref. 29),

$$|S\Sigma\rangle=\sum_{\sigma_a\sigma_b}|s_a\sigma_a\rangle|s_b\sigma_b\rangle\langle s_a\sigma_a s_b\sigma_b|S\Sigma\rangle, \tag{2}$$

where for the $A\,^2\Pi_\Omega$ states in the $^2P+^3P$ limit we have $S=1/2$, $s_a=1/2$, $s_b=1$, and $\Sigma=\Omega-\Lambda$. Following Ref. 30 the product atomic fine-structure states are written as $|j_a\omega_a j_b\omega_b\rangle=|j_a\omega_a\rangle|j_b\omega_b\rangle$ with

$$|j_i\omega_i\rangle=\sum_{\lambda_i\sigma_i}|l_i\lambda_i\rangle|s_i\sigma_i\rangle\langle l_i\lambda_i s_i\sigma_i|j_i\omega_i\rangle,\quad i=a,b. \tag{3}$$

It is now straightforward to compute the transformation matrix elements,

$$\begin{aligned}\langle j_a\omega_a j_b\omega_b|l_a\lambda_a l_b\lambda_b S\Sigma\rangle&\\ =\sum_{\sigma_a\sigma_b}&\langle l_a\lambda_a s_a\sigma_a|j_a\omega_a\rangle\langle l_b\lambda_b s_b\sigma_b|j_b\omega_b\rangle\\ &\times\langle s_a\sigma_a s_b\sigma_b|S\Sigma\rangle,\end{aligned} \tag{4}$$

and the fine-structure branching coefficients $P_{j_a,j_b}^{(\Omega,\lambda_a,\lambda_b)}$ are obtained as

$$P_{j_a,j_b}^{(\Omega,\lambda_a,\lambda_b)}=\sum_{\omega_a\omega_b}|\langle j_a\omega_a j_b\omega_b|l_a\lambda_a l_b\lambda_b S\Sigma\rangle|^2. \tag{5}$$

The results from the last equation are compared to the experimental results and to a purely statistical model in which the statistical multiplicity is assumed to describe the fine-structure distribution.

III. RESULTS

A. Photodissociation versus photodetachment rate

As was shown before,[16] for excitation energies larger than 4.08 eV the dissociation channel opens and the issue of the competition between electron detachment and photodissociation is relevant. Previous work showed a branching ratio of 3% between the two processes (3% PDI versus 97% PDE)[16] in the range of 4.5 eV.

In order to estimate the dissociation versus detachment branching ratio, we have detected the O_2 molecules and the O fragments on the same detector. We employ a 600 V/cm electric field to deflect the parent ion beam after the interaction with laser. This way we ensure that the only fragments that reach the detector are neutral species. By removing a beam dump, the neutral O_2 products are detected in the center of the detector. We found virtually no signal in the absence of the laser light. Figure 2 shows a sample of four datasets recorded at different laser wavelengths between 275 and 285 nm. The particles detected in a confined region (10×10 pixels) in the center of the detector are neutral O_2 products from the photodetachment process. The fragments found outside this small region are O fragments from the photodissociation process. Figure 2 shows that the radius of

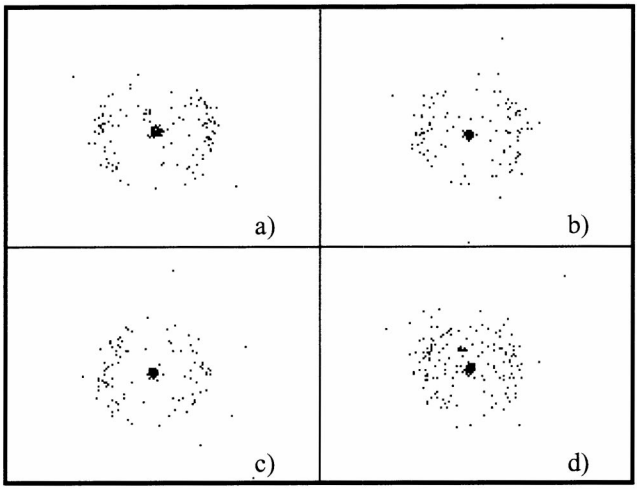

FIG. 2. A 2-D detection of PDE and PDI neutral fragments. The ions (O_2^- and O^-) are deflected away after the laser interaction region and the beam dump is removed. The O_2 fragments from PDE are detected in the central part of the image. The diffuse distribution of particles are O neutrals from PDI. (a) 275 nm; (b) 279 nm; (c) 282 nm; (d) 285 nm.

the O fragment distribution, which is a measure of KER in the dissociation process, increases with photon energy, as expected. We measured the branching ratio of the two processes over the wavelength region of 266–285 nm. The results are plotted in Fig. 3. Detecting both species, O and O_2 on the same detector in a pulse counting mode, makes this result insensitive to small gain differences in the detection of both species. The mean value of the branching ratio is 10%. A linear fit reveals a slight increase in the photodissociation efficiency to higher photon energies.

B. The angular distribution

A second experiment has been performed at 266 nm (4.66 eV) focusing on the photodissociation process itself. This experiment uses coincidence fragment detection, i.e., the photodissociation products O and O^- are recorded in coincidence. A beam dump is placed 20 cm away from the laser interaction region in order to avoid saturation of the

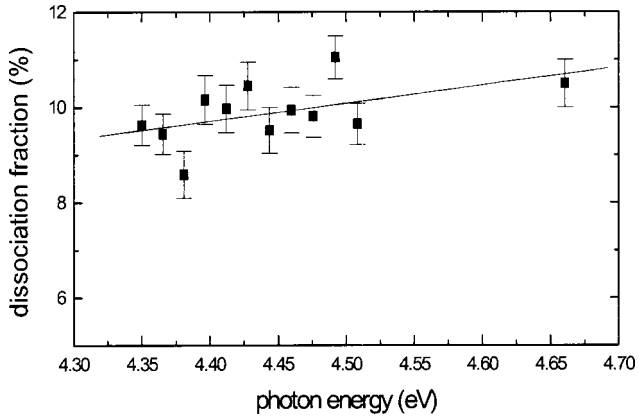

FIG. 3. A fraction of dissociation vs excitation energy. The dissociation fraction is defined as number of O fragments vs the total number of detected particles (O and O_2).

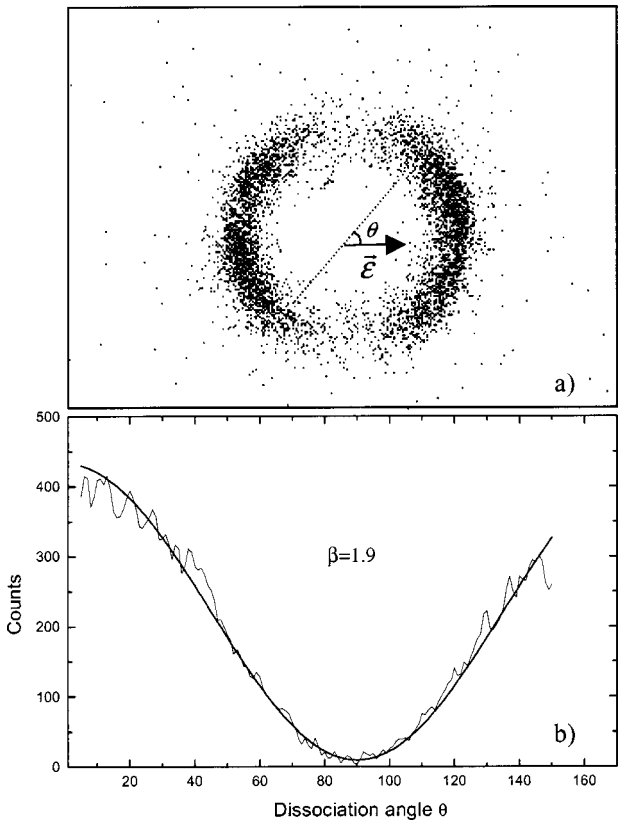

FIG. 4. (a) A sample of raw (x,y) data recorded over 20 000 laser shots at 266 nm. The detection is performed in coincidence ($O+O^-$). The parent O_2^- beam is stopped by the beam dump. The arrow indicates the polarization of the laser; (b) the angular distribution of the fragments. The anisotropy parameter $\beta=1.9$ is obtained by fitting the histogram (thick curve).

central part of the detector, where the main negative ion beam arrives. The beam dump also blocks the neutral O_2 products from the photodetachment process. The raw (x,y) data, as recorded by the camera over 20 000 laser shots at 266 nm, is shown in Fig. 4(a). In this figure, each photodissociation event is represented by two dots on opposite sides of the center of the image. Only one ring is present; it corresponds to one-photon transitions from the ground state $X\,^2\Pi_g(v=0)$ to the continuum of the $A\,^2\Pi_u$ state, generating $O(^3P)+O^-(^2P)$ fragment atoms.

The dissociation process is a direct and fast process via a $A\,^2\Pi_u \leftarrow X\,^2\Pi_g$ parallel transition. To verify this, the angular distribution of the fragments on the detector has been investigated. We recall here the expression for molecular dissociation using linearly polarized light:

$$I(\theta)=\frac{1}{4\pi}[1+\beta(\tau)P_2(\cos\theta)]. \tag{6}$$

Here τ stands for the lifetime of the dissociative state and $P_2(\cos\theta)=3/2\cos^2(\theta)-1/2$. For a direct dissociation process, $\beta_\parallel(\tau=0)=2$ or $\beta_\perp(\tau=0)=-1$, reflecting the character of the transition. In Fig. 4(b) a histogram of the angular distribution of the particles is shown. For each pair of fragments (O and O^-) detected in coincidence and recognized as resulting from the same parent O_2^- by center-of-mass selection, we express the angle θ as the angle between laser polarization and the internuclear axis. The histogram shows a

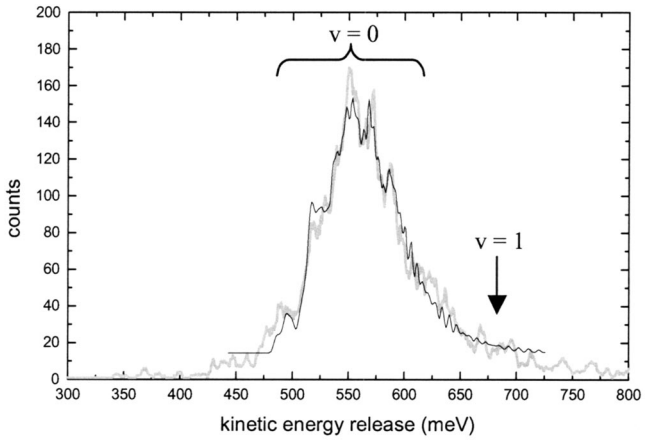

FIG. 5. The KER spectrum (thick gray curve) shows a broad but structured feature around 550 meV associated with transitions from $O_2^-(X\,^2\Pi_{g,\Omega})$ ($\Omega=3/2,1/2$) ($v=0$) states and leading to the $O(^3P_{2,1,0})+O^-(^2P_{3/2,1/2})$ limits. No photofragments starting from $O_2^-(v=1)$ are observed. The fit (thin black curve) is a linear superposition of 12 possible fine-structure transitions and the background line. The results of the fit are presented in Table II.

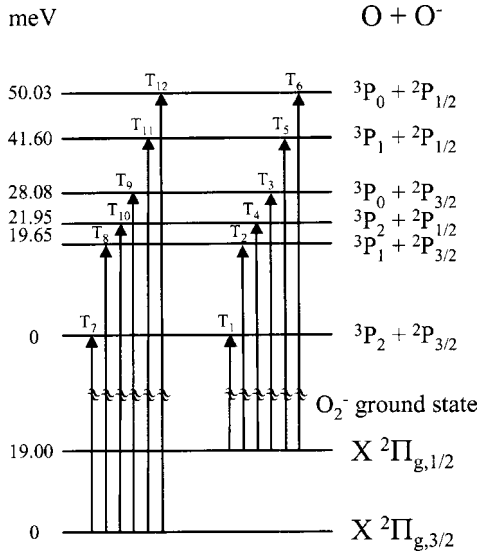

FIG. 6. The diagram shows the fine structure of the ground state of O_2^- and of the dissociation limit ($O+O^-$). The arrows indicate the transitions used in the fitting of the KER spectrum. The relative energies are expressed in meV.

sudden decrease of signal around 165°. This is an unfortunate consequence of the presence of the beam dump; the angular region from 150° to 175° degrees is hidden by the holder of the beam dump (data not shown). The solid curve is the best fit of the histogram (ignoring the region mentioned above). We have used for the fit the function expressed in Eq. (6). The anisotropy parameter β derived from the fit equals 1.9 ± 0.02, where the error gives the fitting uncertainty. Uncertainties on the absolute background level implies that our result is not inconsistent with $\beta=2$. This result supports very well the belief that the dissociation happens via a $A\,^2\Pi_u \leftarrow X\,^2\Pi_g$ parallel transition.

C. Experiment: The fine-structure at the dissociation limit

In our experiment, the full kinematics of the dissociation process are obtained via a three-dimensional coincidence detection. This information makes possible the identification of the initial state as well as the fine structure of the dissociation limit, by means of KER spectra. For each coincidence event, KER is calculated:

$$\mathrm{KER}=\frac{E_0}{4L^2}(D^2+v_0^2\,\Delta t^2), \tag{7}$$

where E_0 is the kinetic energy of the parent beam (5 keV), L is the length of the flight tube from the region where dissociation takes place to the detector, D is the distance measured on the detector between the two fragments, Δt is the arrival time difference of the particles and v_0 is the velocity of the parent beam. Figure 5 shows a histogram of the observed KER distribution. As the spatial resolution of the apparatus is better than the temporal one, the resolution of the KER determination is increased by employing a further selection of events. We select only events with a minimum time difference and a maximum spatial separation. These events are dissociations in the plane parallel to the detector. The observed KER values in the broad peak reveal that photodissociation starts from different rotational and fine-structure levels of the ground state $X\,^2\Pi_g(v=0)$, leading to the $O(^3P_{2,1,0})+O^-(^2P_{3/2,1/2})$ limits. The near absence of a $v=1$ dissociation peak around 670 meV as well as $v=2$ dissociation peak around 800 meV reveals the absence of $X\,^2\Pi_g(v=1,2)$ levels in the initial ion beam or a dissociation probability that decreases very strongly with the vibrational quantum state, which is not very likely. This result is surprising in view of the expected stability of $O_2^-(v=1)$ and $O_2^-(v=2)$ states.

The superoxide ion has two spin–orbit ground states $O_2^-(X\,^2\Pi_{g,\Omega})$ ($\Omega=3/2,1/2$), which are split by $A=-20\pm2$ meV.[2] The lowest ground state is $O_2^-(^2\Pi_{g,3/2})$. The dissociation limit $O(^3P_j)+O^-(^2P_{j^-})$, in fact, forms a manifold of six dissociation limits. The fine-structure splitting of $O(^3P_{2,1,0})$ is accurately known ($<10^{-4}\,\mathrm{cm}^{-1}$) from laser magnetic-resonance experiments.[25–28] The $^3P_1$ and $^3P_0$ levels are 19.65 and 28.08 eV, respectively, above the $^3P_2$ level. For the $O^-(^2P_{3/2,1/2})$ fine-structure splitting, we have used the latest high precision result 177.084(14) cm^{-1} (21.95 meV), which has been obtained using photodetachment microscopy.[10] Figure 6 shows 12 possible transitions and relative energies of the fine-structure states used in the simulation of the KER spectrum. The transition T_{12} originating from $O_2^-\,X\,^2\Pi_{g,3/2}$ and ending on the dissociation limit $O(^3P_0)+O^-(^2P_{1/2})$ does not conserve the projection of total angular momentum, exclusive of nuclear spin on the molecular axis, but it is considered in the fit and found to contribute. The rotational population of the anion ground state of $O_2^-(X\,^2\Pi_g)$ is assumed to obey a thermal distribution. Considering the temperature of the ion source $T=350\,\mathrm{K}$ and the rotational constant $\beta_e=1.16\,\mathrm{cm}^{-1}$, up to $R=35$ rotational states are populated. The shape of each transition used in the fitting of the KER spectrum is

TABLE I. The diabatic and statistical model for the branching over the 12 transitions.

Transitions	Ω	j	j^-	KER[a] meV	Diabatic %	Statistical %
T_1	1/2	2	3/2	573	0.1852	0.3704
T_2	1/2	1	3/2	553	0.3333	0.2222
T_3	1/2	0	3/2	545	0.1481	0.0741
T_4	1/2	2	1/2	551	0.0926	0.1852
T_5	1/2	1	1/2	531	0.1667	0.1111
T_6	1/2	0	1/2	523	0.0741	0.0370
T_7	3/2	2	3/2	554	0.5556	0.3704
T_8	3/2	1	3/2	534	0.1111	0.2222
T_9	3/2	0	3/2	526	0	0.0741
T_{10}	3/2	2	1/2	532	0.2778	0.1852
T_{11}	3/2	1	1/2	512	0.0556	0.1111
T_{12}	3/2	0	1/2	504	0	0.0370

[a]The maximum of the calculated KER distribution corresponding to a photon energy of 4.66 eV.

$$T_i(\Omega,j,j^-,x) = \sum_R (2R+1) * e^{-\beta_e R(R+1)/kT} * e^{-(x-\mathrm{KER})/2\sigma^2}. \quad (8)$$

KER is the kinetic energy release, taking into account the initial rotational state and the different asymptotic channels, as defined by R, Ω, j, and j^-. The KER resolution of the detector and imaging equals ($\sigma=2$ meV). The Earth's magnetic field as well as stray electric fields affect the trajectories of the charged O^-. We actively compensate for this effect by employing a small electric field. Nevertheless, a small residual shift remains: $d\sim 400\,\mu$m. Since the O and O^- fragments cannot be distinguished on the detector, the effect of magnetic field appears as an apparent splitting of each KER peak, one at KER corresponding to a distance between fragments $D-d$ and the other one at KER corresponding to a distance $D+d$. The splitting is ~31 meV. This effect is included in the shape of the transitions considered in the fit. The calculated maxima of the KER distribution for each transition, ignoring this instrumental complication, are presented in Table I. Not all of the 12 combinations (see Table I) of the two molecular ground states and the six dissociation limits, T_i, are individually resolved. Only seven groups of lines, G_i, are distinguished (see Table II). For example, transitions T_5, T_8, and T_{10} corresponding to almost the same KER are grouped together and taken into account in the fit as one line, G_4.

TABLE II. Fit coefficients for the branching.

Obs. Lines	Transitions	Fit coefficients %	Diabatic %	Statistical %
G_1	T_{12}	0.06±0.01	0	0.0185
G_2	T_{11}	0.08±0.01	0.0278	0.0555
G_3	T_6+T_9	0.06±0.03	0.0370	0.0555
G_4	$T_5+T_8+T_{10}$	0.33±0.02	0.2778	0.2592
G_5	T_3	0.02±0.03	0.0740	0.0370
G_6	$T_2+T_4+T_7$	0.29±0.03	0.4907	0.3889
G_7	T_1	0.16±0.03	0.0926	0.1852

In the simulation of the KER spectrum we have used a least square linear fitting routine. The input matrix consists of the 7 KER distributions representing the 12 transitions, G_i. A small constant background is added to account for the minor fraction of accidental coincidences. The detection of multiple coincidences per laser shot opens the possibility of recording accidental coincidences; an incorrect combination of two fragments coming from different dissociation events but having an apparent center of mass in the region of acceptance for true coincidences. The best fits were obtained using 19 meV for the fine-structure splitting in the superoxide anion ground state. We note that the observed structures in Fig. 5 could only be consistently fitted using the known energy differences between the dissociation limits and the known instrumental parameters. This observation corroborates the origin of the observed structure in the KER peak. The error bars have been determined by fitting 100 realizations of the spectrum while changing the spectrum randomly within the statistical uncertainty per channel, on top of determining the sensitivity of the fit results toward changes in other parameters, such as the 19 meV fine-structure splitting, and the rotational temperature in the range of $T_r^{\mathrm{fit}} = 300-350$ K. We find that the data are best described limiting the fine-structure splitting to 19±1.5 meV.

Table I also shows the calculated, theoretical results using the diabatic model described above, as well as the results of a simple statistical model. A fully adiabatic dissociation would result in population of the first dissociation limit, $O(^3P_2)+O^-(^2P_{3/2})$, only. With respect to the calculations, we note that the results of the diabatic model predict a significant larger population of the excited $O(^3P_J)$ states than the statistical in the case of the superoxide anion ground state, whereas the reverse is the case starting from the excited O_2^- ($\Omega=1/2$) anion state. As can be deduced from Table I, the sum of the diabatic predictions, starting from the two molecular states and leading to a certain dissociation limit are identical to the statistical prediction. This remarkable observation cannot be general, since a necessary condition for this observation is that the selection rules allow the molecular state to connect to all possible dissociation limits. Certain allowed molecular symmetries do not meet this condition. At this moment, we have no explanation of this effect.

Table II and Fig. 7 show the comparison between the experimentally deduced branchings and the theoretical ones. Here some individual transitions have been grouped, as described above. Note that the groups are numbered with increasing KER value, whereas the transitions are numbered, as described in Table I. The experimental results are represented by the fit coefficients. For the comparison, we have adopted equal populations for both molecular fine-structure states. Unfortunately, we cannot deduce this population ratio directly from the data. We note that no *a priori* information has been used in the experimental fit. A very nice agreement is found between the calculated and predicted trends in the branching. The superoxide anion clearly does not dissociate adiabatically. It is, however, difficult to distinguish between the diabatic and the statistical model. Finally, we note that we observe a small contribution for G_1. This dissociation pathway does not conserve the projection Ω in going from

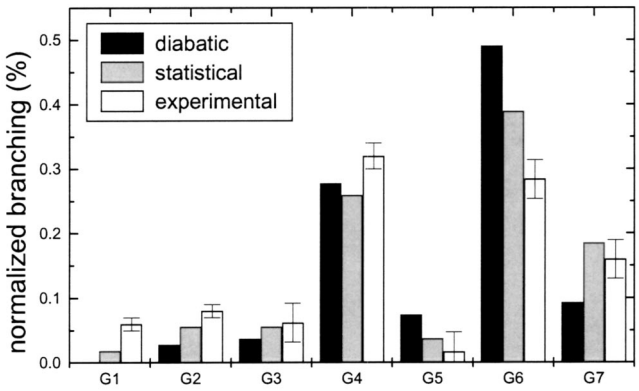

FIG. 7. The experimental branchings over the seven groups of transitions (white columns) are compared with a diabatical calculation (black columns) and the statistical model (gray columns).

the molecule ($\Omega=3/2$) to the highest dissociation limit, $O(^3P_0)+O^-(^2P_{1/2})$ with total $\Omega=1/2$.

IV. DISCUSSION

A. Photodetachment mechanism

We have found a dissociation fraction of approximately 10% slowly increasing with photon energy over a wavelength region between 285 and 266 nm. We have established that the dissociation process starts from $O_2^- X\,^2\Pi_{g,1/2,3/2}(v=0)$ states only and that it takes place via the continuum of $A\,^2\Pi_u$, based on the anisotropy parameter. Finally, we have obtained information on the correlated product state information. First, we will discuss the photodetachment process, which can proceed via a number of pathways, both direct and indirect:

$$O_2^-(X\,^2\Pi_g)+h\nu \rightarrow O_2(X\,^3\Sigma_g^-, a\,^1\Delta_g, b\,^1\Sigma_g^+)+e^-, \quad (9)$$

$$\rightarrow O_2(c\,^1\Sigma_u^-)+e^-, \quad (10)$$

$$\rightarrow O_2^-(A\,^2\Pi_u)$$

$$\rightarrow O_2(X\,^3\Sigma_g^-, a\,^1\Delta_g, b\,^1\Sigma_g^+)+e^-, \quad (11)$$

$$\rightarrow O_2^-(A\,^2\Pi_u) \rightarrow O_2(c\,^1\Sigma_u^-)+e^-, \quad (12)$$

where Eqs. (9) and (10) refer to direct processes while Eqs. (11) and (12) refer to indirect processes, better described as the autodetachment of the photoexcited intermediate $O_2^-(A\,^2\Pi_u)$ state. Two processes, Eqs. (10) and (12), have their energetic threshold at $\lambda\sim275$ nm. The dominant valence electron configurations of the states involved are the following: $\pi_u^4\pi_g^3$ for the $O_2^-(X\,^2\Pi_g)$ state, $\pi_u^4\pi_g^2$ for the $O_2(X\,^3\Sigma_g^-, a\,^1\Delta_g, b\,^1\Sigma_g^+)$ states; $\pi_u^3\pi_g^3$ for the $O_2(c\,^1\Sigma_u^-)$ state; and $\pi_u^3\pi_g^4$ for the $O_2^-(A\,^2\Pi_u)$ state.[6] Equations (9), (10), and (12) are one-electron processes; Eq. (11) is indirect and involves a two-electron process in the autodetachment step. Equation (12) is the result of two one-electron processes, but has a very small Franck–Condon overlap in the autodetachment step at our excitation energies.

An absolute determination of the efficiencies of these pathways is not easy. The observed photodissociation fraction may reflect the relative cross sections of direct photodetachment and molecular excitation. However, a photodetachment signal due to autodetachment of the excited molecular anion state cannot be ruled out based on our observations. The measurements of the branching fraction, fine-structure distribution and anisotropy presented here do not contain direct information on the origin of the observed branching fraction. Bailey *et al.* concluded from studying autodetachment studies via bound vibrational levels in the $O_2^-(A\,^2\Pi_u)$ state that the absorption cross section to this state may well be equal to the photodissociation cross section.[4] The observation of vibrational structure in this experiment is suggestive for autodetachment lifetimes being much longer than a vibrational period. As a consequence, upon excitation molecular dissociation would be much faster than autodetachment.

In fact, an electron energy spectrum of the photodetached electrons could be more revealing in this respect. Autodetachment via the dissociative $O_2^-(A\,^2\Pi_u)$ state should result in a change in the Franck–Condon factors with different product neutral O_2 vibrational levels. We have not found measurements in the literature in this direction. Further, it is of interest to note that the photodissociation branching does not change upon energetically opening of the reaction channels associated with Eqs. (10) and (12). Opening of these channels could increase the relative autodetachment rate and decrease the dissociation fraction.

Theory is more revealing in unraveling the different mechanisms. Recently, multichannel scattering calculations were performed,[5] providing cross sections for the photodetachment of O_2^-, leading to O_2 for photon energies up to 50 eV. Since this theoretical work was performed using a fixed nuclei approximation, the cross sections should be seen as total absorption cross sections. The distribution of the total cross section shows an overall smooth increase for photon energies up to 20 eV followed by a smooth and slower decrease toward an energy of 50 eV. The only prominent structure is a resonance appearing at photon energies between 5 and 6 eV (the cross section increases locally by a factor of 4 up to $15-20\times10^{-18}\,\mathrm{cm}^2$). The resonance has the configuration of $1\pi_u^3 1\pi_g^{45}$ and it is attributed to the $O_2^-(A\,^2\Pi_u)$ state. Our experiment was performed in a wavelength region (4.35–4.66 eV) and the total theoretical cross section should be around $4.5\times10^{-18}\,\mathrm{cm}^2$. The main contributions to this cross section are processes of Eq. (9) [$\sim2\times10^{-18}\,\mathrm{cm}^2$ for $O_2(X\,^3\Sigma_g^-)\leftarrow O_2^-(X\,^2\Pi_g)$, $\sim1.5\times10^{-18}\,\mathrm{cm}^2$ for $O_2(a\,^1\Delta_g)\leftarrow O_2^-(X\,^2\Pi_g)$, $\sim1\times10^{-18}\,\mathrm{cm}^2$ for $O_2(b\,^1\Sigma_g^+)\leftarrow O_2^-(X\,^2\Pi_g)$]. All three partial cross section distributions in the 11-channel calculation leading to $O_2(X\,^3\Sigma_g^-, a\,^1\Delta_g, b\,^1\Sigma_g^+)$ states show the same resonance around 5 eV. The resonance has a configuration of $1\pi_u^3 1\pi_g^4$ and it is attributed to the $O_2^-(A\,^2\Pi_u)$ state. Our experiment probes the low-energy wing of this resonance. It is tempting to interpret the small increase in photodissociation fraction as the increase of this resonance. This would imply that at these energies the $O_2^-(A\,^2\Pi_u)$ state, once populated, decays mainly via dissociation processes, and it accounts for the high dissociation rate of 10%.

The contribution of the $O_2(c\,^1\Sigma_u^-)\leftarrow O_2^-(X\,^2\Pi_g)$ [see Eq. (10)] is small in this wavelength region, as well as the

contribution of Eq. (12) (according to the one-channel calculation, the maximum cross section of this reaction is obtained for a photon energy of 10 eV). The rest of the states taken into account in this theoretical work show various maxima for photon energies higher than 10 eV and do not contribute significantly to the total cross section for photon energies below 5 eV.

As the photodetachment mechanism is likely to be dominated by a direct one-photon process as well, we describe our experiment by

$$\begin{aligned} &O_2^-(X\,^2\Pi_g)+h\nu(266-285\ \text{nm})\\ &\quad\rightarrow O_2(X\,^3\Sigma_g^-, a\,^1\Delta_g, b\,^1\Sigma_g^+)+e^- \quad (\sim 90\%)\\ &\quad\rightarrow O_2^-(A\,^2\Pi_u)\rightarrow O(^3P_j)+O^-(^2P_j) \quad (\sim 10\%). \end{aligned} \tag{13}$$

It is tempting to conjecture that at the peak of the 5 eV resonance, photodissociation may even dominate over photodetachment.[5] A preliminary experiment at a photon wavelength of 212 nm (5.8 eV) did not show any increase in the photodissociation fraction. The 212 nm has been obtained by frequency mixing of the fourth harmonic of the Nd:YAG (266 nm) with the fundamental wavelength of the same laser (1064 nm). It is possible that at this increased energy the autodetachment process via the $O_2(c\,^1\Sigma_u^-)$ state has increased significantly in strength, reducing the photodissociation rate.

B. The fine-structure of the dissociation limit

In general, the transition from the chemical and exchange forces at short range via the long range atomic interactions to the asymptotic limit, where the atomic fine-structure splitting is the dominating splitting, is considered a complex issue. This process has regained interest because of the field of cold collisions, in which long range interactions and small angular momentum values dominate the collision dynamics. Accurate diabatic predictions on the photodissociation process are possible because of the molecular structure of the superoxide anion. The present system is relatively simple, because at large internuclear separations (1–2 nm) the molecular potentials are well described by electrostatic charge–quadrupole interactions between the atoms, whereas the spin–orbit interaction still can be neglected. In more heavy systems, the projection on the asymptotic atomic states may involve already Hund's case-*c* wave functions, a situation that complicates the determination of some of the matrix elements that are important for the final diabatic picture.[32] It should be noted that the charge–quadrupole interaction in O_2^- is stronger than the quadrupole–quadrupole interaction in neutral O_2. Hence, in comparing the anion with the neutral, the dissociation behavior could have been more adiabatic in the anionic case. However, the two systems both seem to be rather diabatic in dissociation behavior.[34]

Understanding the dissociation dynamics of diatomic molecules implies being able to predict the distribution over the different fine-structure states. This type of research has not received a lot of attention because of the relatively small number of experiments that could be performed at this level of detail. With the improvements in ion imaging techniques, such as velocity map imaging,[33] experiments at this detail for important atmospheric molecules may well become possible; see, for example, Ref. 34 on molecular oxygen. Using velocity map imaging, no correlated fine-structure information in the case of oxygen has been reported.

Coincident fast beam photofragment techniques have been able to obtain quantitative correlated information on the atomic fine-structure states employing the aspect of coincident detection. The experiment reported by Leahy *et al.* is an excellent example of how coincidence experiments can reveal details of the photodissociation of molecular oxygen via the Schumann–Runge states.[31] The complexity of the Schumann–Runge predissociation process and the fact that their theory required a small number of fitting parameters, makes it harder to draw firm conclusions. The present study of the superoxide anion is a favorable case for theoretical calculations. The dissociation process involves one dominant molecular state and the description of the charge–quadrupole interaction makes it possible to generate a diabatic model without any parameter. The experimental resolution reached in the present experiment was not sufficient to determine accurate branching fractions that can be compared quantitatively. The data show that dissociation is far from adiabatic and much closer to diabatic and statistical models. The presence of dissociation fragments at the channel that does not conserve Ω in the dissociation can not be explained within the present diabatic model.

The importance of the superoxide anion in atmospheric sciences resides dominantly in the chemistry in the upper atmosphere. In this region, the UV flux is intense. The reported 10% photodissociation should not be neglected in ionosphere models. Photodissociation of the superoxide anion is a source of the atomic anion, which may play a role in the upper atmosphere.

ACKNOWLEDGMENTS

The work described in this paper is part of the research program of the Foundation for Fundamental Research on Matter (Stichting voor Fundamenteel Onderzoek der Materie) and it was financially supported by the Netherlands Organization for Scientific Research (Nederlandse Organisatie voor Wetenschappelijk Onderzoek) through the FOM-program Molecular Atmospheric Processes. We thank Dr. R. R. Lucchese for discussions on his calculations.

[1] R. J. Celotta, R. A. Bennet, J. L. Hall, M. W. Siegel, and J. Levine, Phys. Rev. **5**, 631 (1972).
[2] M. J. Travers, D. C. Cowles, and G. B. Ellison, Chem. Phys. Lett. **164**, 449 (1989).
[3] J. Rolfe, W. Holzer, W. F. Murphy, and H. J. Bernstein, J. Mol. Spectrosc. **26**, 543 (1968).
[4] C. G. Bailey, D. J. Lavrich, D. Serxner, and M. A. Johnson, J. Chem. Phys. **105**, 1807 (1996).
[5] P. Lin and R. R. Lucchese, J. Chem. Phys. **114**, 9350 (2001).
[6] M. Krauss, D. Neumann, A. C. Wahl, G. Das, and W. Zemke, Phys. Rev. A **7**, 69 (1973).
[7] K. P. Huber and G. Herzberg, *Molecular Spectra and Molecular Structure: Constants of Diatomic Molecules* (Van Nostrand-Reinhold, New York, 1979).
[8] H. Hotop and W. C. Lineberger, J. Phys. Chem. Ref. Data **4**, 539 (1975).
[9] D. M. Neumark, K. R. Lykke, T. Andersen, and W. C. Lineberger, Phys. Rev. A **32**, 1890 (1985).

[10] C. Blondel, C. Delsart, C. Valli, S. Yiou, M. R. Godefroid, and S. Van Eck, Phys. Rev. A **64**, 052504 (2001).
[11] R. W. Schunk and A. F. Nagy, *Ionospheres—Physics, Plasma Physics and Chemistry* (Cambridge University Press, Cambridge, 2000).
[12] D. S. Burch, S. J. Smith, and L. M. Branscomb, Phys. Rev. **112**, 171 (1958).
[13] P. C. Cosby, R. A. Bennett, J. R. Peterson, and J. T. Moseley, J. Chem. Phys. **63**, 1612 (1975).
[14] P. C. Cosby, J. H. Ling, J. R. Peterson, and J. T. Moseley, J. Chem. Phys. **65**, 5267 (1976).
[15] M. L. Vestal and G. H. Mauclaire, J. Chem. Phys. **67**, 3758 (1977).
[16] D. J. Lavrich, M. A. Buntine, D. Serxner, and M. A. Johnson, J. Chem. Phys. **99**, 5910 (1993).
[17] R. J. Van Brunt and L. J. Kieffer, Phys. Rev. A **2**, 1899 (1970).
[18] P. D. Burrow, J. Chem. Phys. **59**, 4922 (1973).
[19] T. F. O'Malley, Phys. Rev. **155**, 59 (1973).
[20] G. Das, A. C. Wahl, W. T. Zemke, and W. C. Stwalley, J. Chem. Phys. **68**, 4252 (1978).
[21] G. Das, W. T. Zemke, and W. C. Stwalley, J. Chem. Phys. **72**, 2327 (1980).
[22] L. Dinu, A. T. J. B. Eppink, F. Rosca-Pruna, H. L. Offerhaus, W. J. van der Zande, and M. J. J. Vrakking, Rev. Sci. Instrum. **73**, 4206 (2002).
[23] D. Strasser, X. Urbain, H. B. Pedersen, N. Altstein, O. Heber, R. Wester, K. G. Bhushan, and D. Zajfman, Rev. Sci. Instrum. **71**, 3092 (2000).
[24] R. Bobbenkamp, Ph.D. thesis, Bielefeld, 2002.
[25] R. J. Saykally and K. M. Evenson, J. Chem. Phys. **71**, 1564 (1979).
[26] P. B. Davies, B. J. Handy, E. K. Murray Lloyd, and D. R. Smith, J. Chem. Phys. **68**, 1135 (1978).
[27] J. O. Hirschfelder, C. F. Curtiss, and R. B. Bird, *Molecular Theory of Gases and Liquids* (Wiley, New York, 1954).
[28] G. Scoles, *Atomic and Molecular Beam Methods* (Oxford University Press, Oxford, 1988), Vol. 1.
[29] M. C. G. N. van Vroonhoven and G. C. Groenenboom, J. Chem. Phys. **116**, 1954 (2002).
[30] M. C. G. N. van Vroonhoven and G. C. Groenenboom, J. Chem. Phys. **116**, 1965 (2002).
[31] D. J. Leahy, D. L. Osborne, D. R. Cyre, and D. M. Neumark, J. Chem. Phys. **103**, 2495 (1995).
[32] S. J. Singer, K. F. Freed, and Y. B. Band, J. Chem. Phys. **79**, 6060 (1983).
[33] A. T. J. B. Eppink and D. H. Parker, Rev. Sci. Instrum. **68**, 3477 (1997).
[34] B. Buijsse, W. J. van der Zande, A. T. J. B. Eppink, D. H. Parker, B. R. Lewis, and S. T. Gibson, J. Chem. Phys. **108**, 7229 (1998).